Surfaces and Interfaces 38 (2023) 102793

Contents lists available at ScienceDirect

Surfaces and Interfaces

journal homepage: www.sciencedirect.com/journal/surfaces-and-interfaces

Original concept of cracked template with controlled peeling of the cells perimeter for high performance transparent EMI shielding films

A.S. Voronin [a,b,c,*], Y.V. Fadeev [a,b], F.S. Ivanchenko [a], S.S. Dobrosmyslov [a,b], M.O. Makeev [c], P.A. Mikhalev [c], A.S. Osipkov [c], I.A. Damaratsky [c], D.S. Ryzhenko [c], G.Y. Yurkov [c,d], M.M. Simunin [a,b,e], M.N. Volochaev [f], I.A. Tambasov [b,f,g], S.V. Nedelin [b,f,g], N.A. Zolotovsky [b,f,g], D.D. Bainov [h,i], S.V. Khartov [a]

[a] Federal Research Center «Krasnoyarsk Scientific Center, Siberian Branch, Russian Academy of Sciences» (FRC KSC SB RAS), Krasnoyarsk, Russia 660036
[b] Siberian Federal University, Krasnoyarsk, Russia 660041
[c] Bauman Moscow State Technical University, Moscow Russia 105005
[d] N.N. Semenov Federal Research Center of Chemical Physics of Russian Academy of Sciences, Moscow, Russia 119334
[e] Reshetnev Siberian University Science and Technology, Krasnoyarsk, Russia 660037
[f] Kirensky Institute of Physics, Siberian Branch, Russian Academy of Sciences, Krasnoyarsk Russia 660036
[g] LLC Research and Production Company "Spectehnauka", Krasnoyarsk, Russia 660043
[h] Tomsk Polytechnic University, Tomsk, Russia 634050
[i] V.E. Zuev Institute of Atmospheric Optics, Siberian Branch, Russian Academy of Sciences, Tomsk, Russia 634055

ARTICLE INFO

Keywords:
Transparent conductor
Cracked template
Cells perimeter peeling
EMI shielding films

ABSTRACT

The problem of sputtering of thick metal films on micro and nanotemplates is important for obtaining mesh transparent conductors with excellent optoelectric characteristics. In this work, we demonstrate for the first time the possibility of controlling the degree of peeling of the cell perimeter from the substrate for a cracked template based on egg white by alternating the operations of moistening the template with saturated water vapor and shock drying with hot air. Local peeling of the cracked template cells perimeter makes it possible to increase the thickness of the metal sputtered on the cracked template by more than 1 μm, which is not achievable for other lithographic approaches. Our technique was used to obtain thick Ag meshes with a low sheet resistance of no more than 1.59 Ω/sq and a transparency of about 89.1%. The thick Ag meshes show a shielding efficiency (*SE*) of 49 dB or 99.998% of the incident power of an electromagnetic wave at a frequency of 1 GHz. In a sandwich geometry, thick Ag meshes, which simulates a real shielding window, the shielding efficiency (*SE*) reaches 71 dB with a transparency of more than 80%.

1. Introduction

In the modern world, the space surrounding a person is permeated with electromagnetic waves of various ranges. Parasitic electromagnetic microwave radiation can interfere with the correct operation of communication systems, precision measuring equipment, human life support systems (for example, pacemakers), as well as work in special programs. Also, according to numerous studies, non-ionizing microwave radiation in the frequency range of 0.1–300 GHz is a factor in provoking serious diseases in humans [1,2]. Recently, the attention of a large number of scientific teams has been paid to the development of shielding materials that can effectively reduce the negative factor of electromagnetic interference [3,4].

Electromagnetic shielding of transparent objects such as computer monitors, displays of precision measuring equipment and building glazing has a big impact on information security [5]. As transparent shielding coatings for microwave radiation, the most promising are metal micro- and nanostructures, which include micro- and nanometer-scale meshes obtained using photolithography (PL) [6–9], imprint lithography [10,11], self-organization [12–15], 3D printing methods [16,17] and electrohydrodynamic jet printing [18]; Ag and Cu nanowires films [19–22]; as well as thin-film coatings with the

* Corresponding author at: Federal Research Center «Krasnoyarsk Scientific Center, Siberian Branch, Russian Academy of Sciences» (FRC KSC SB RAS), Krasnoyarsk, Russia 660036.
E-mail address: a.voronin1988@mail.ru (A.S. Voronin).

https://doi.org/10.1016/j.surfin.2023.102793
Received 29 December 2022; Received in revised form 15 February 2023; Accepted 2 March 2023
Available online 5 March 2023

TCO/Me/TCO [23,24] structure.

Metal meshes provide a shielding efficiency of more than 40 dB or a shielding of 99.99% of the power with a transparency of more than 80%. The high shielding efficiency is due to the low sheet resistance. An increase in *SE* relative to currently obtained results can be achieved by forming a metal based transparent conductor with a sheet resistance of less than 0.5 Ω/sq, taking into account that the fill factor (*FF*) should be no more than 15% to ensure acceptable transparency, it is necessary to increase network structure thickness up to 500 nm and more. As a rule, templates formed by photolithography methods, as well as by self-organization processes, have restrictions on the thickness of the sputtered metal, which does not exceed 300 nm [12,25,26]. These limitations are associated with the formation of a continuous film of metallization during the sputtering process, due to the fusion of the metal sputtered on the bottom of the template and the side face of the cell. As a result, when the template is removed, the mesh structure is damaged. The problem of obtaining thick mesh transparent conductors by vacuum metal sputtering methods is typical for all types of templates, both lithographic and self-assembled. In photolithography, this problem is solved in two ways: the first method is the formation of an acute angle between the substrate and the side faces of the photomask cells [27]; the second method is the use of a positive photoresist followed by etching of the cells of the network structure [6,28]. Based on the fact that there are now a limited number of solutions for solving this problem, it is important to develop approaches for alternative lithographic template structures that make it possible to form meshes transparent conductor with a thickness of more than 1 μm.

It is important to note that there is an effective technique for increasing the thickness of mesh transparent conductors, which are produced by galvanic growing of Cu or Ni films on a seed mesh obtained using various templates [29–32]. This method is interesting because of the possibility of obtaining coatings with an extremely low sheet resistance of less than 0.1 Ω/sq; however, an additional technological cycle does not always have a positive effect on economic costs. In this regard, one-stage methods for obtaining transparent conductors based on thick metallic meshes are attractive.

In this work, for the first time, we propose a technique for cyclic exposure of the cracked template to moist and hot dry air, which provides local peeling of the cells perimeter. In the process of metal sputtering on templates with a peeling cells perimeter prevents the formation of a conformal metal film. Using a cracked template with peeling cells perimeter, Ag meshes with a thickness of more than 1 μm can be obtained on a flexible PET substrate.

2. Materials and methods

2.1. Materials

Egg white, egg yolk obtained from food market. Ag (99,99%), Cr (99,99%) targets Kurt J. Lesker (USA). PET film 50 μm thick manufactured by HiFi 747 (HiFi, UK) were used as substrates. PMMA thick sheets (Röhm GmbH, Germany) were used as spacers, the thickness of which was 1, 2, and 4 mm.

2.2. Cracked template preparation

To ensure strong adhesion of the cracked template, the PET substrate was pre-treated with a corona discharge using an Arcotec folienstation FER-B coronator (Arcotec GmbH, Germany). The value of the corona discharge current varied from 0 to 45%. The surface energy of the PET substrate was controlled using Accu Dyne Test (USA) test markers.

Egg white was used as a precursor to form the cracked template. A liquid egg white layer was deposited onto a PET substrate using the slot die coating method. The thickness of the of egg white layer to obtain a cracked template was 20, 30 and 40 μm. After deposition, the egg white liquid layer was dried at room temperature - 20 °C and humidity - 55%.

2.3. Forming cracked template with peeled cells perimeter

In the moistening step, we use saturated water vapor. The moistening time of the cracked template was 3, 5, and 7 s. The technique has an iterative character. Decreasing the exposure time leads to insufficient moisture, which results in insufficient template response to shock drying. Externally, the template is slightly different from the original.

In the experiment, we considered the temperature range with an acceptable response to shock drying, which was 100–140 °C, the time of one shock drying iteration was 5 s.

2.4. Magnetron sputtering

Silver was used to form a metal mesh transparent conductor, the sputtering thicknesses were 600, 1000, 1500 and 2500 nm. Argon with a purity of 99.99% was used as a working gas. Argon was supplied to the working chamber through a mass flow controller. The working chamber was evacuated using a turbomolecular pump. The residual and working gasses pressure was $2.3 \bullet 10^{-3}$ Pa and $2.2 \bullet 10^{-1}$ Pa, respectively. Power to the magnetron sputtering system was supplied from a unit generating DC pulses with a frequency of 133 kHz. Sputtering took place in the mode of stabilization of the discharge power, which was maintained at a level of 1 kW. In this case, the discharge current was 2.7 A.

A quartz sensor was used to control the silver films thickness by measuring the resonant frequency change.

2.5. Formation of shielding sandwich structures

The procedure for forming a two-layer sandwich structure was as follows: at the first stage, 0.1 ml of HOA 63 was applied to the reverse side of the Ag mesh on a PET substrate with dimensions of 3 × 3 cm. From above, a drop was distributed using a PMMA spacer with different thicknesses of 1, 2, or 4 mm. The same operation was repeated for the opposite side of the sandwich structure. The resulting sandwich structure was pressed for 1 min with a force of 100 N. After that, without relieving pressure, the sandwich structure was exposed to UV radiation (20 W, $\lambda = 365$ nm) for 10 min.

2.6. Microscopic study

The morphology of the cracked templates and different thick Ag meshes was studied by optical and scanning electron microscopy (SEM) using TM 4000 (Hitachi, Japan), with the accelerating voltage 15 kV, and Hitachi S5500 (Japan) with the accelerating voltage 3 kV. SEM equiped with an energo-dispersive X-Ray spectrometer XFlash 430 (EDX, Brucker, USA).

Geometrical characteristics of cracked template and thick Ag meshes were calculated from 10 images, cells sizes and cracks width were averaged.

Visualization of cells with a peeled perimeter and thick Ag meshes based this cracked templates was carried out in the cross-section mode. For this purpose, cross-sectional samples of cracked templates without peeling of the cells perimeter, after one iteration cells perimeter peeling and after two iterations cells perimeter peeling as well as thick Ag meshes based this cracked templates were prepared by focused ion beam (Ga+, 40 kV) single-beam FIB system FB-2100 (Hitachi, Japan). The image in the cross-section mode was obtained by scanning ion microscopy (SIM) FB-2100 (Hitachi, Japan).

The local surface morphology and thickness of meshes were determined by atomic force microscopy (AFM), SmartSPM-1000 (AIST-NT, USA). For best results, scanning was carried out in semi contact mode using high-resolution cantilevers NSG10 with a tip curvature radius of 10 nm.

2.7. Optoelectric study

The spectral dependencies of the optical transmittance of the thick Ag meshes were measured in the range of 400–700 nm with a spectrophotometer UV-3600 (Shimadzu, Japan).

A four-probe method was used for sheet resistance measurements using a Keithley 2000 multimeter (Keithley, USA) and a four-probe head 854–22–004–10–001,101 (Mill-Max, USA).

2.8. Adhesion strength, mechanical and long-term stability

The adhesion strength of thick Ag meshes studied using a tape test according to ASTM D 3359, in geometry B (notch lattice period was 2 mm). The effect of the reusable tape test on sheet resistance and *SE* also studied. 3 M tape was used in all studies.

The mechanical properties of Ag meshes were studied in comparative experiments at a laboratory stand in a cyclic mode. Cyclic bending allows exploration of the accumulation of fatigue in meshes. In our experiments, the number of bending cycles with a radius of 5 mm was 1000.The mechanical properties of Ag meshes were studied in comparative experiments at laboratory stands.

The long-term stability of thick Ag meshes to external conditions was studied in two modes. The first mode is a monthly exposure of thick Ag meshes at satureted humidity and room temperature, which was 20 °C. The second mode is a weekly exposure thick Ag meshes at a temperature of 85 °C and a saturated humidity. The experimental procedure was as follows: a small container with distilled water was placed in a glass with a ground-in lid to maintain satureted humidity. Then the test sample was placed in the container and autoclaved according to the above test protocols. The value of the sheet resistance of the coating was used as an evaluation criterion.

2.9. EMI shielding measurements

In this study, the *SE* of the materials was measured using a special 16.00/6.95 mm air-filled coaxial cell (type II, 50 Ω, GOST RV 51,914–2002). The advantages of this approach are a wide frequency range (from 10 MHz to 7 GHz), the ability to measure at low frequencies and a relatively simple and convenient measurement technique. It is required to ensure reliable electrical contact between the material sample and the conductors of the coaxial path over the entire area of their contact for the correctness of the result. To overcome this difficulty, the specific design of the cell has a groove of varying thickness into which the sample is inserted and clamped. Electro-sealing gaskets made of dense metallized fabric were used for better electrical contact between the sample and the coaxial tract walls. The cell provides the correct result for conductive samples.

The test bench includes a FieldFox N9916A (Keysight, USA) network analyzer, coaxial cable assemblies and a cell; we performed a full two-port calibration at the cell inputs. To determine the *SE* of a material sample:

1 measure the spectrum S_{21} (or S_{12}) of the cell without a sample (groove thickness-0 mm), S_{21OS} (dB),
2 measure the spectrum S_{21} (or S_{12}) of the sample cell, S_{21S} (dB),
3 calculate the spectrum *SE* (dB) by formula (1),

$$SE = S_{21OS} - S_{21S} \quad (1)$$

The dynamic measurement range of the *SE* unit is 80 dB and the measurement error is ± 2 dB.

3. Result and discussion

3.1. Concept cracked template with peeling of the cells perimeter

The initial stage of formation of a cracked template based on egg white is described in detail in our previous works [31,32]. The main idea of this work is the hypothesis that the cracked template cells can be partially bent with followed by peeled perimeter during cycling of moistening – shock drying iterations. Schematically, the process of partial peeling of the perimeter of the cracked template cells and the features of sputtering of an silver film on such templates are shown in Fig. 1.

The proposed technological process can be described based on the following considerations. The egg white that makes up the cracked template is a hygroscopic material. If you place the cracked template in an atmosphere with high humidity, the egg white layer absorbs moisture from the air, increasing its volume. First of all, moisture is absorbed in the surface layer of the egg white and then gradually diffuses deep into the cell. In the process of shock drying, moisture from the surface layers evaporates more actively than from the deeper ones. Therefore, a gradient of egg white shrinkage occurs in the cell volume. The shrinkage gradient generates mechanical stresses that tend to bend the edges of the cell. The cell perimeter is torn off when the generated mechanical stresses exceed the adhesion forces of the cell to the substrate. At the same time, the adhesion forces of the cell perimeter decrease at the stage of moisturizing the egg white layer, because moisture from the air enters the template cells mainly along their perimeter. The height of the rise of the edge of the template cell above the substrate depends on the parameters of the template moistening, the parameters of the shock drying, and the thickness of the cracked template. After complete drying, the bend of the edges of the cells is fixed in a predetermined position. Repeating iterations of moistening and shock drying is one way to increase the area of the peripheral part of the template cells that hangs over the substrate. From the point of view of the morphological features of the sprayed mesh, in the process of peeling of the cells perimeter of the cracked template, the evidence of this process is the change in the cross section of the path from rectangular to trapezoidal.

3.2. Selection of optimal parameters and analysis of the geometric characteristics of cracked template with cells perimeter peeling

If we consider the literature results, then in the article [33] the morphogenesis of the peeling of the cells perimeter for cracked layers of latex was studied in detail. The effect of layer thickness, drying rate, and solvent type on the process of peeling the cells perimeter was considered. The key parameter influencing the peeling of the cells perimeter is the adhesion of the cracked material to the substrate.

At the first stage, we studied the relationship between the surface energy of the PET substrate and the morphology of the cracked template. On Fig. 2 shows the dependence of the surface energy of the PET substrate on the magnitude of the corona discharge current and the morphology of the cracked template for the PET substrate with different surface energies.

The dependence of the surface energy has the form of two straight lines. With an increase in the corona discharge current from zero to 20%, no increase in the surface energy of the PET film is observed. The morphology of a cracked template formed on a PET substrate having a surface energy of 30 din/cm (corona discharge current of 15%) is shown in Fig. 2b. An inhomogeneous cracks width is observed, blind cracks and generally cracked template has poor adhesion. Such a cracked template is not technologically advanced, its cells can peel off during storage, transportation and metal sputtering. Increasing the surface energy of the PET substrate to 36 din/cm (the corona discharge current is 25%) demonstrates an increase in cracked template quality (Fig. 2c). The photograph clearly shows interference rings along the perimeter of the cells, which is associated with a partial peeling of their perimeter.

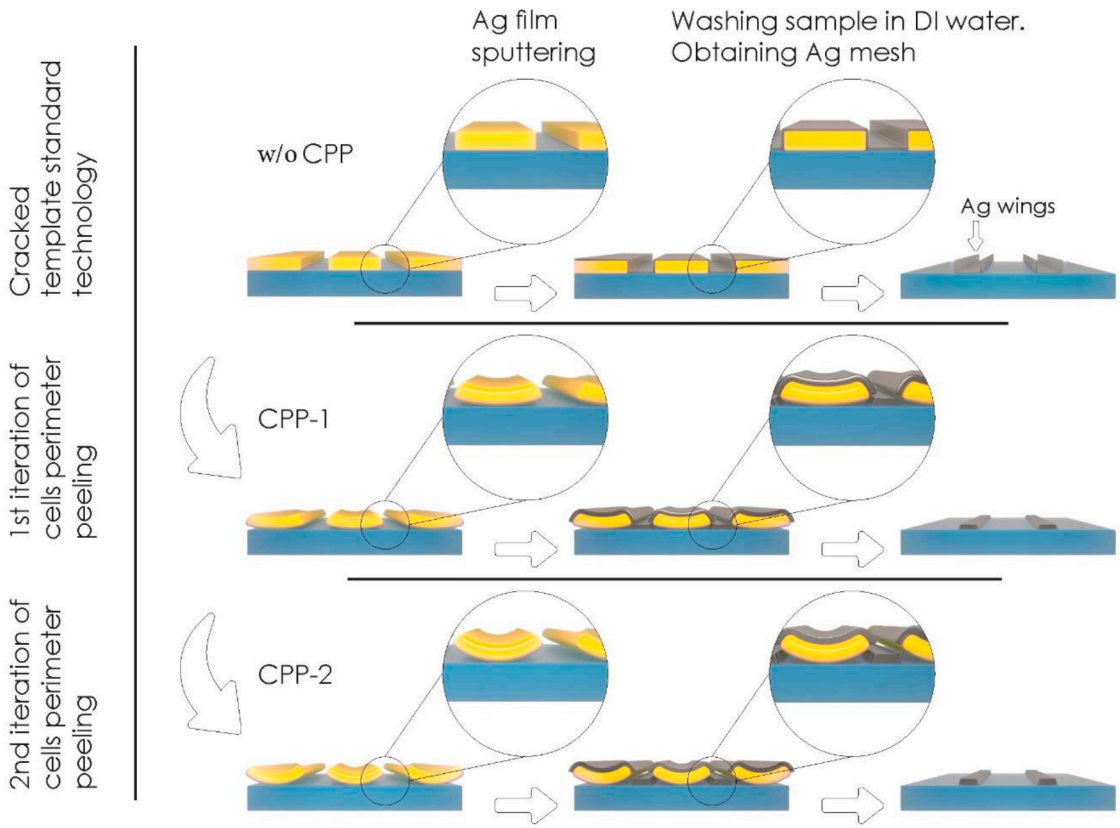

Fig. 1. Schematic representation of the process of peeling of the cells perimeter of cracked template and features of silver sputtering on such templates.

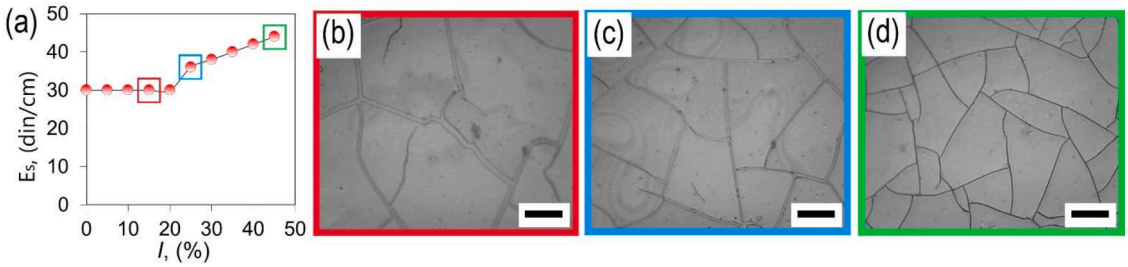

Fig. 2. Dependence of the surface energy of the PET substrate on the corona discharge current (a); Optical images cracked template on substrates with different surface energies: 30 din/cm (b) (red square on the plot); 36 din/cm (c) (blue square on the plot) and 44 din/cm (d) (green square on the plot) (scale bar 50 μm).

However, the amount of peeling of the cells perimeter is quite large, as evidenced by the fact that the area of the region with the observed interference is larger than the circle with strong adhesion to the substrate [33]. Some heterogeneity is also observed, i.e. the perimeter of some cells is peeled more than others. Further increasing the surface energy of the PET substrate to 44 din/cm (the corona discharge current is 45%) demonstrates the cracked template as being the most suitable for laboratory and industrial formation of transparent conductor meshes (Fig. 2d). In further work, to form a cracked template, we used a PET substrate treated with a corona discharge with a the current of 45%.

In addition to the adhesion of the template to the substrate, two parameters are important for the operation of peeling the cells perimeter. The first parameter is the cracked template moistening time. We use saturated water vapor for it. The optimal moistening time was determined experimentally; three values of 3, 5, and 7 s were considered. The shock drying temperature was fixed at 120 °C, the shock drying time was 5 s. The number of moistening-shock drying iterations was two. Fig. S1 shows photographs of cracked templates for two iterations of cells perimeter peeling. It can be seen that the optimal moistening time is 3 s. Decreasing the moistening time results in poor template response. Outwardly, it differs slightly from the original. Increasing the exposure time to 5 s (Fig. S1) leads to over moistening of the cracked template. Merging of the thinnest cracks related to the secondary and subsequent stages of cracked template evolution is observed [34]. When the moistening time is increased to 7 s, coalescence of the main fractures can be observed, i.e. the percolation of the fracture network is disturbed (Fig. S1).

The second key parameter influencing the process of obtaining a cracked template with a peeled cells perimeter is the air temperature during the shock drying process. The temperature should be high to create maximum mechanical stresses in each individual cell of the cracked template, but also should not lead to hardening of the egg white layer, which will complicate its washing at the stages of obtaining a mesh transparent conductor. The temperature range with an acceptable response to shock drying was experimentally determined. We considered the shock drying temperature range of 100–140 °C, (Fig. S2).

After determining the appropriate parameter vector, the target line of cracked templates was formed. The coating thickness of the liquid egg

white layer was 20, 30, and 40 μm. The main goal was to study the change in the geometric characteristics of the cracked template with different thicknesses (Fig. S3).

Fig. 3 shows SEM images of a cracked template, where the thickness of the liquid layer of egg white is 40 μm, without cells perimeter peeling (w/o CPP, Fig. 3a), after one iteration of cells perimeter peeling (CPP-1, Fig. 3b) and two iterations of cells perimeter peeling (CPP-2, Fig. 3c), respectively.

According to SEM images (Fig. 3a-c), the main conclusions can be drawn about the evolution of the cracked template during the peeling of the cells perimeter. First, the operation of peeling the perimeter of the cells leads to a decrease in the average cells size. This occurs due to additional cracking for the relaxation of mechanical stresses accumulated as a result of moistening- shock drying iterations. Secondly, an increase in the width of the cracks is observed due to the peeling of the cells; as a result, the projection of the cell onto the substrate plane becomes smaller.

Using the cross-section images shown in the insets (Fig. 3a-c), we can judge the increase in the distance between the PET substrate and the cell perimeter within one crack. Cracked template w/o CPP does not show the presence of interference rings inside the cells according to optical photographs (Fig. S3g), however, detailed analysis of cross-section images (Fig. S4a and S4b) demonstrate the presence of a defective zone, which consists in local peeling of the cells perimeter, accompanied by tearing of the PET substrate. The width of the defect zone does not exceed 1 μm; the height of the cell overhanging the PET substrate is no more than 300 nm. For the CPP-1 template, the width of the perimeter peeling zone increases, according to our estimates, to 5 μm; the maximum peeling value is observed at the corners of the cell (Fig. S4h). Cross-section images (Fig. S4 c,d) show both an increase in the cell overhang over the PET substrate, which is about 1 μm, and an increase in peeling zone width. The CPP-2 template shows a distinct presence of interference rings inside the cells (Fig. S4i). For this type of template the width of the peel zone exceeds 10 μm, the cell overhang over the PET substrate mare when 1.5 μm (Fig. S4 e,f).

Based on the SEM data, a statistical analysis of the cracked template of various thicknesses, before and after the peeling of the cells perimeter, was carried out. There is a trend associated with a decrease in the average cells size (Fig. 3d) and an increase in the width of the cracks (Fig. 3e), typical for all thicknesses of the egg white layer. For all thicknesses of the egg white layer, the value of 1-*FF* (Fig. 3f) has similar values due to the fact that a smaller cracked template thickness corresponds not only to a smaller cells size, but also to a smaller cracks width. These templates correlate well with the literature results described in publications on cracked template [12,35–38] and on cracking in droplets of colloidal solutions in general [39,40].

3.3. Morphological study of thick Ag meshes based on cracked template with peeling of the cells perimeter and their optoelectrical properties

At the stage of magnetron sputtering of thick silver films, morphological features appear, showing a significant difference between the w/o CPP, CPP-1 and CPP-2 templates. The formation of a continuous film of metal is easy to follow at the stage of washing. Fig. S5a shows photographs of sample based on a cracked template without peeling of the cells perimeter the process of soaking in DI water for 5 min, the thickness of the silver film is 1500 nm. It can be seen that the cracked template, which has not been subjected to the process of peeling the perimeter of the cells, swells with bubbles. SEM images show the fusion of the silver film belonging to the side face of the template and the path (Fig. S5b and S5c). At the same time, for the cracked template CPP-2, the cells perimeter peeling makes the swelling process uniform, and the washing process separates single cells (Fig. S5a).

On Fig. 4a shows SEM images of Ag meshes based on various cracked templates with sputtered silver thicknesses of 600, 1000, 1500, and 2500 nm. The green frame highlights the acceptable metal thicknesses at which the Ag mesh has no defects, the red highlights the silver thickness that are unacceptable for this type of template.

The operation of peeling the perimeter of the cells makes it possible to sputtering a thicker film of silver. Thus, for the w/o CPP template, a high-quality coating was obtained only at thicknesses of 600 and 1000 nm, at thicknesses of 1500 and 2500 nm (SEM images of Ag meshes with an unacceptable silver thickness have a red frame), multiple damage to the mesh structure is observed, associated with the merging of the path with the sputtered metal on the side face of the cells, the so-called "wings" [27]. The CPP-1 template makes it possible to increase the

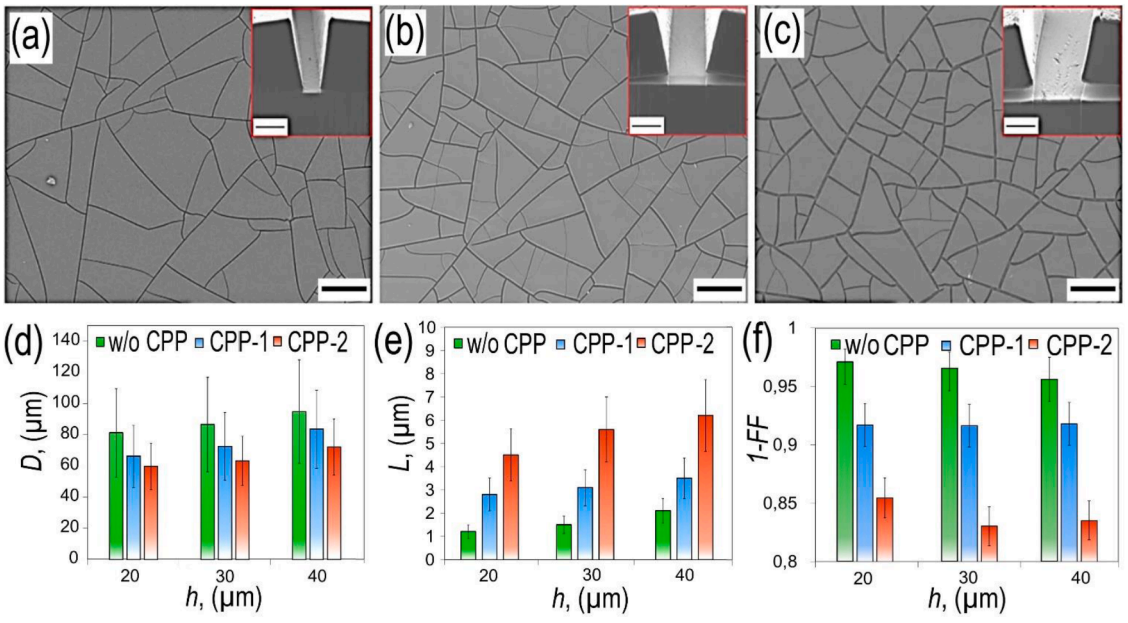

Fig. 3. SEM image cracked template (egg white layer thickness 40 μm) at various stages: w/o CPP (a); CPP-1(b); CPP-2 (c) (scale bar 100 μm); The insets show cross-section images of the cracked template-PET substrate interface at various stages of cell perimeter peeling: w/o CPP (d); CPP-1(e); CPP-2 (f) (scale bar 3 μm); Statistical analysis of mean cells size (d); average cracks width (e); the value of 1-*FF* (f) for cracked template, its dependence on the thickness of egg white layer and the number of iterations of peeling the perimeter of the cells.

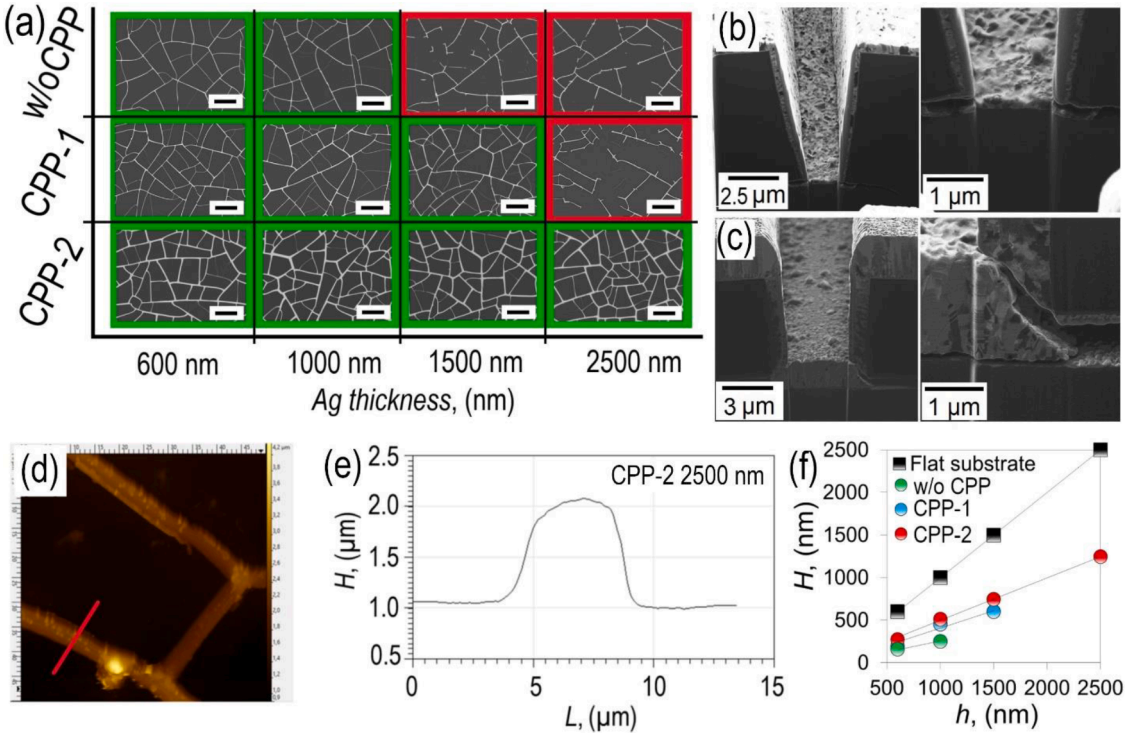

Fig. 4. SEM images of different thickness Ag meshes based templates with varying degrees of peeling of the cells perimeter (a); Cross-section images 600 nm Ag sputtering on to template w/o CPP (b); Cross-section images 2500 nm silver sputtering on to template CPP-2(c); AFM images and profiles Ag mesh CPP-2 2500 nm (d, e); Relationship between the thickness of the sputtered silver and the actual thickness of the Ag meshes for various cracked templates (f).

thickness of the sputtered silver up to 1500 nm. For the CPP-2 template, the formation of "wings" was not observed even for silver sputtering with a thickness of 2500 nm.

Cross-sectional examination of samples w/o CPP 600 nm (Fig. 4b) and CPP-2 2500 nm prior to the wash process shows significant differences in morphology. For the w/o CPP cracked template, even 600 nm silver causes spacing problems between the path and the film belonging to the side face of the cell (Fig. 4b). Meanwhile, for the CPP-2 template, even at the maximum silver thickness, there is a clear separation between the path and the film belonging to the side face of the cell (Fig. 4c).

The local morphology and actual thickness of the Ag meshes based on the above cracked template was determined by the AFM method. AFM images and profiles for Ag meshes CPP-2 with a sputtering thickness of 2500 nm are shown in Fig. 4d and Fig. 4e, respectively. Based on the actual thickness of the Ag meshes, it can be concluded that only a part of the sputtered metal reaches the bottom of the crack.

Fig. 4f shows plots of Ag meshes thickness vs. sputtered film thickness. According to the results of linear approximation, the coefficient of metal mass transfer to the cracks bottom is 25.44% (w/o CPP), 40.71% (CPP-1) and 49.82% (CPP-2). The maximum thickness of the Ag mesh CPP-2 coating is 1.13 μm at a sputtered silver thickness of 2500 nm. Obviously, the transfer coefficient is related to the aspect ratio of the fracture, according to our estimates based on cross-section data, for the w/o CPP template, the value is L/H~0.33, for the CPP-1 template, an increase in L/H to ~0.58 is observed, finally for template CPP-2, this value is L/H~1. In the process of controlled peeling of the cells perimeter, we also observe an increase in the aspect ratio of cracks, as a result of which the coefficient of mass transfer of metal to the bottom of the cracks increases.

Figs. 5a and Fig. S6 shows the appearance of the Ag mesh CPP-2 1500 nm A4 sample format and cracked template CPP-2 roll sample. The main goal is to demonstrate the fact that the operation of peeling of the cells perimeter of the cracked template is uniform over the entire area of the sample and is reproducible. On Fig. 5b shows optical transmission in the range 400–780 nm for Ag meshes based on templates w/o CPP, CPP-1 and CPP-2 with 600 nm silver thickness. It is worth noting that we are operating with a transparency value that applies only to the Ag mesh transparent conductor, i.e. we do not take into account the losses associated with the PET substrate, which has a transmission value in the considered range of ~87% (Fig. S7). The optical transmission of the mesh transparent conductor has a constant value over the entire wavelength range under consideration and is related to the *Fill Factor*. For regular meshes, transparency can be estimated from the equation

$$T = 1 - FF = \frac{(D-L)^2}{D^2} \quad (2)$$

there D is the period of the mesh, L is the width of the path. Based on this formula, we can estimate the optical transparency for our Ag meshes. Based on Eq. (2), the transparency of the Ag mesh based on the w/o CPP template should be 95.6% (Fig. 3f), measured to be 95.2% transparency. For Ag meshes based on templates CPP-1 and CPP-2, with a silver sputtering thickness of 600 nm, it is 90.1% and 82.5% (Fig. 5b), respectively, while the transparency estimated from purely geometric considerations is 91.7% and 83.5% (Fig. 3f).

On Fig. 5c shows the sheet resistance measurements at ten different points, for Ag meshes with the maximum thickness of the sputtered silver, for all types of cracked template. It can be seen that the maximum deviation observed for the Ag mesh w/o CPP 1000 nm sample is about 9.7%, the average sheet resistance value is 5.5 Ω/sq. The average sheet resistance for the Ag mesh CPP-1 1500 nm is 1.59 Ω/sq, the maximum deviation is 27.04%, this is possibly caused by damage to the Ag mesh. Ag mesh CPP-2 2500 nm has an average sheet resistance of 0.28 Ω/sq, the maximum deviation from the average is 11.6%.

Fig. 5d shows the parameters of all thick Ag meshes obtained in this work and their comparison with promising transparent conductors obtained in the literature. Cracked template w/o CPP as the thickness of the sputtered silver increases from 600 nm to 1000 nm, the transparency

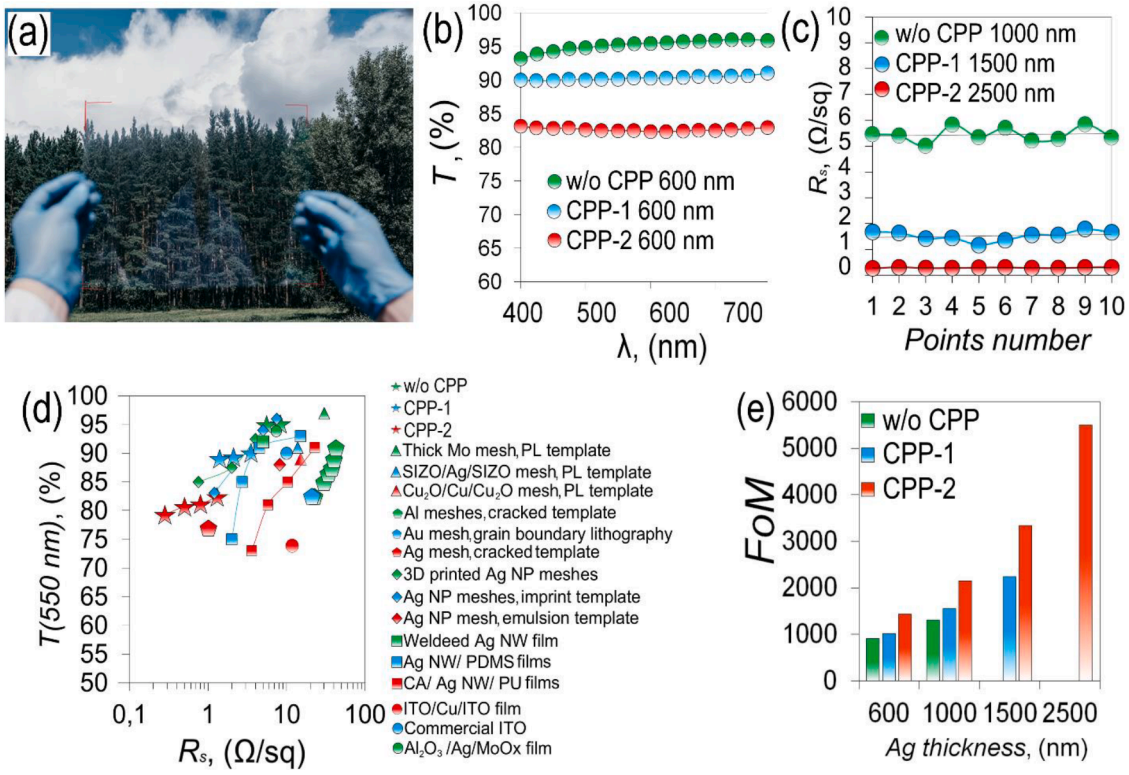

Fig. 5. External view of the sample based on the CPP-2 template 1500 nm, A4 format (a); Spectral dependence of optical transmission for Ag meshes 600 nm thick, for cracked templates w/o CPP, CPP-1 and CPP-2 (b); 10 point sheet resistance measurement for Ag meshes with maximum silver thickness, for templates w/o CPP, CPP-1 and CPP-2 (c); Optical transmission as a function of sheet resistance. For comparison, different high performance transparent conductor: thick Mo mesh, PL template [27]; SIZO/Ag/SIZO mesh, PL template [41]; Cu_2O/ Cu/ Cu_2O mesh, PL template [42]; Al mesh, cracked template [43]; Au mesh, grain boundary template [44], Ag mesh, cracked template [45]; 3D printed Ag NP mesh embedded in PDMS [46], Ag NP mesh, imprint template [10], Ag NP mesh, emulsion template [15]; welded Ag NW film [47]; Ag NW/PDMS films [48]; CA/Ag NW/ PU films [21]; Al_2O_3 /Ag/ MoO_x film [49]; ITO/ Cu/ ITO film [50] (d); Dependence of *FoM* on Ag sputtering thickness for all types of templates (e).

decreases from 95.1 to 95% with a decrease in sheet resistance from 8.3 Ω/sq to 5.55 Ω/sq. For the CPP-1 template, an increase in the silver thickness from 600 to 1500 nm i.e. 2.5 times led to a decrease in transparency from 90.1% to 89.1%, while the sheet resistance decreased from 3.68 Ω/sq to 1.59 Ω/sq. In the case of the CPP-2 template, as the metal thickness increases from 600 nm to 2500 nm, the optical transmission decreases from 82.5% to 79.3%, while the sheet resistance decreases from 1.41 Ω/sq to 0.28 Ω/sq. All mesh samples retain high integrity, as evidenced by the absence of "wings" in the SEM data. Increasing the thickness of the metal does not have a strong effect on the transparency of the Ag meshes (Fig. 5d). Also in Fig. 5d compares thick Ag meshes based on cracked templates with peeled of the cells perimeter with literature data for transparent conductors of various geometry and structures. The plot shows metal meshes based on PL templates [27,41, 42], self-organization templates [43–45], imprint lithography templates [10,46], and Ag NW`s films [21,47,48] and TCO/Me/ TCO films [49, 50].

A universal characteristic for transparent conductors is the *Figure of Merit* (*FoM*), which is a universal function depending on optical transmission and sheet resistance for a transparent conductor as well. *FoM* is defined by the equation [51]

$$FoM = \frac{Z_0}{2R_s\left(\frac{1}{\sqrt{T}} - 1\right)} \tag{3}$$

On Fig. 5f shows the *FoM* values for all obtained in the framework of Ag meshes. It can be seen that even for a cracked template without cells perimeter peeling, Ag meshes w/o CPP 1000 nm has a transparency of 95% at a sheet resistance of 5.55 Ω/sq, which corresponds to a *FoM* value of more than 1303, this value is typical only for the highest quality transparent conductors. For Ag mesh based template CPP-2 with silver thickness 2500 nm, the *FoM* value is 5495, previously the coatings obtained by vacuum sputtering methods did not show such a high *FoM* value. Only metal mesh transparent conductors obtained by electrochemical methods have a greater *FoM* value [29–31].

3.4. EMI shielding performance of single thick Ag meshes and sandwich structures

The *SE* value is related to the transmission coefficient *T* by the following equation $SE = -T$, so we can characterize the shielding coating by the *SE* value by taking the experimental value of the coefficient *T* with the opposite sign.

As a rule, the shielding ability of a transparent conductor has a strong dependence on its sheet resistance. For shielding films whose thickness is less than the skin layer thickness, the shielding efficiency can be calculated using the thin layer model

$$SE = 20\lg\left(1 + \frac{Z_0}{2R_s}\right) \tag{4}$$

Eq. (4) is in good agreement with experiment for continuous (TCO and TCO/ Me/ TCO films [24]) and quasi-continuous coatings (for example, for Ag and Cu NW`s films [21,22]) in the GHz frequency range.

A schematic representation of a coaxial measuring stand with a sample placed in it is shown in Fig. 6b.

The frequency dependence of the *T* coefficient for Ag mesh based on templates w/o CPP (Fig. 6c), CPP-1 (Fig. 6d) and CPP-2 (Fig. 6e) is typical for metal mesh transparent conductors. In the entire studied range, a monotonous increase in the *T* coefficient is observed, that is, a

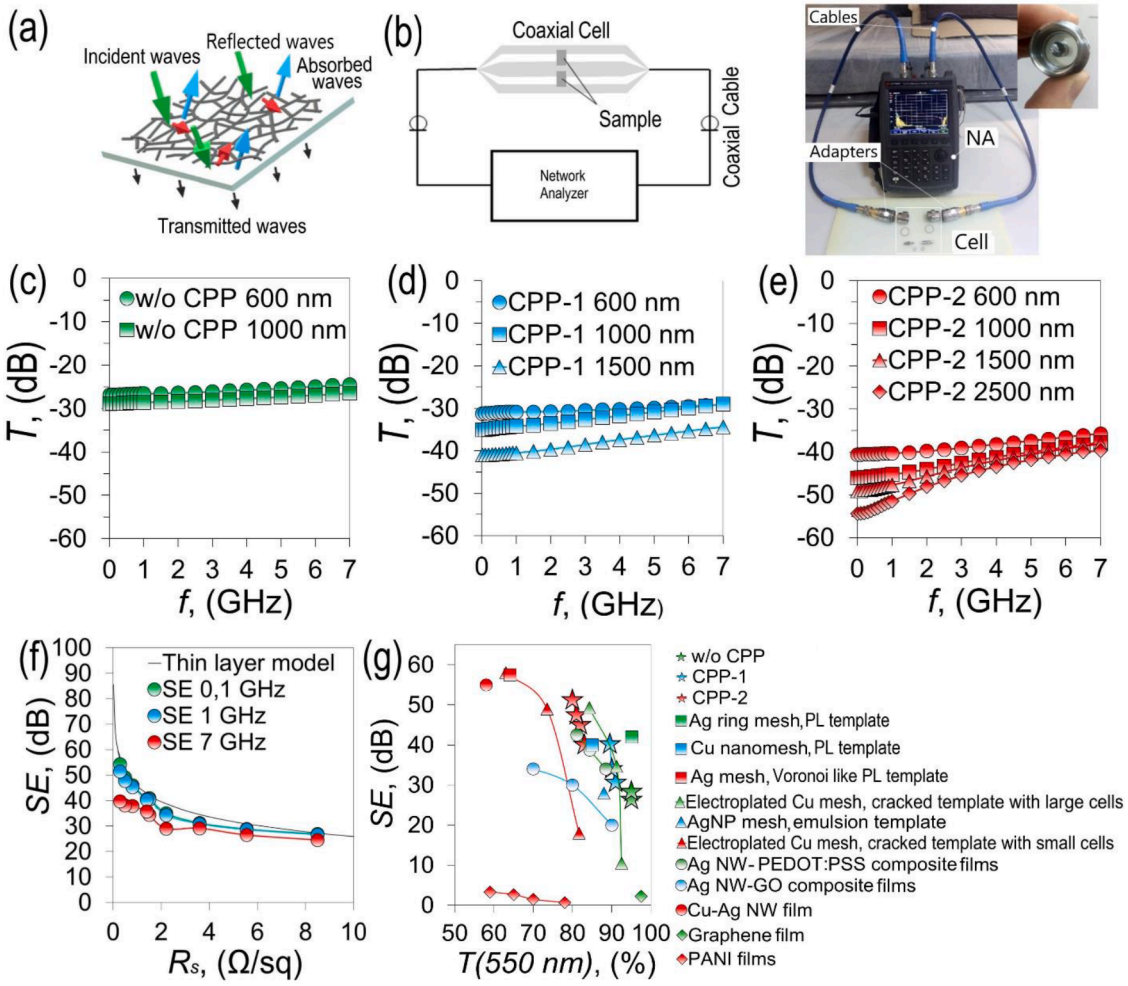

Fig. 6. Schematic representation of the interaction of microwave radiation with Ag meshes based on cracked template with CPP (a); Schematic representation and photo of a measurement cell using a coaxial waveguide line (b); Spectral transmission in the range 0.01–7 GHz for thick Ag meshes based on w/o CPP (c), CPP-1 (d) and CPP-2 (e) cracked template; Comparison of *SE* according to the thin layer model with *SE* for various Ag meshes (f); *SE* values at 1 GHz as a function of optical transmittance. For comparison, the *SE* value of Al ring mesh [53], Cu nanomesh [6], Voronoi like Ag mesh [54], based PL templates; electroplated Cu meshes, based cracked template with small and large cells [32], Ag NP mesh, emulsion template [15]; Ag NW-PEDOT:PSS [55] and Ag NW-GO composite films [56], Cu-Ag NW film [56]; graphene film [58], PANI films [59] (g).

uniform decrease in *SE*. Moreover, the less Ag meshes has sheet resistance, the greater the slope. For Ag mesh w/o CPP 1000 nm, the value of *T* at a frequency of 10 MHz is −28.87 dB, at a frequency of 7 GHz, the value of *T* is −26.49 dB, i.e., the difference at the boundaries of the studied range is 2.38 dB. With a decrease in sheet resistance, for example, for Ag mesh CPP-2 2500 nm, the difference *T* at the boundaries of the studied range is 14.69 dB. This behavior of the frequency dependence of *T* is typical for mesh transparent conductors with a cells size of more than 50 μm; agreement with the thin layer model is observed only at frequencies not exceeding 1 GHz (Fig. 6f) and is consistent with the literature results [31,32]. At higher frequencies, there is a discrepancy with the thin layer model. The reason for the discrepancy between the experimental results and the model is diffraction effects. Mesh transparent conductor, can be represented as an array of irregular holes in a metal screen. For perforated screen, the maximum shielding efficiency can be calculated according to the equation [52]

$$SE_{app} = 20\lg\left(\frac{\lambda}{2d}\right) - 10\lg(n) + 32\frac{t}{w} \quad (5)$$

there *d* is the maximum linear size of the hole; *n* is the number of holes at a distance of λ/2; *t*/*w* is the ratio of the thickness (*t*) to the width (*w*) of the screen. However, in the case of an array of closely spaced holes, if the distance is much smaller than the aperture width, the film behaves like a single aperture and can be estimated using the first term in Eq. (5).

The comparative dependence of *SE* at 1 GHz on transparency at a wavelength of 550 nm is shown in Fig. 6g, the most promising transparent conductors were chosen as objects of comparison - metallic meshes based PL templates [6,53,54], self-organized templates [15,32], films based on Ag NW`s such as Ag NW-PEDOT:PSS [55] and Ag NW-GO [56] composite films, electroplated Cu-Ag NW film [57], as well as graphene [58] and PANI films [59]. Analysis of the comparative plot shows that our Ag meshes based on cracked template with cells perimeter peeling are in the leading group of samples in all ranges of optical transparency.

The concept of shielding sandwich structures is an obvious way to increase the *SE* while maintaining an acceptable optical transparency. The literature considers shielding sandwich structures consisting of two or more layers of metallic transparent conductors separated by a dielectric spacer [60–62]. In sandwich structures, an increase in *SE* is observed due to the successive interaction of the incident microwave radiation with two transparent conductors. In a shielding sandwich structure, resonances similar to those in a Fabry-Perot interferometer can be observed [63]. The resonant wavelength depends on the thickness of the sandwich structure (the distance between the reflective films) and on the permittivity of the spacer [64]. On Fig. 7a shows a schematic

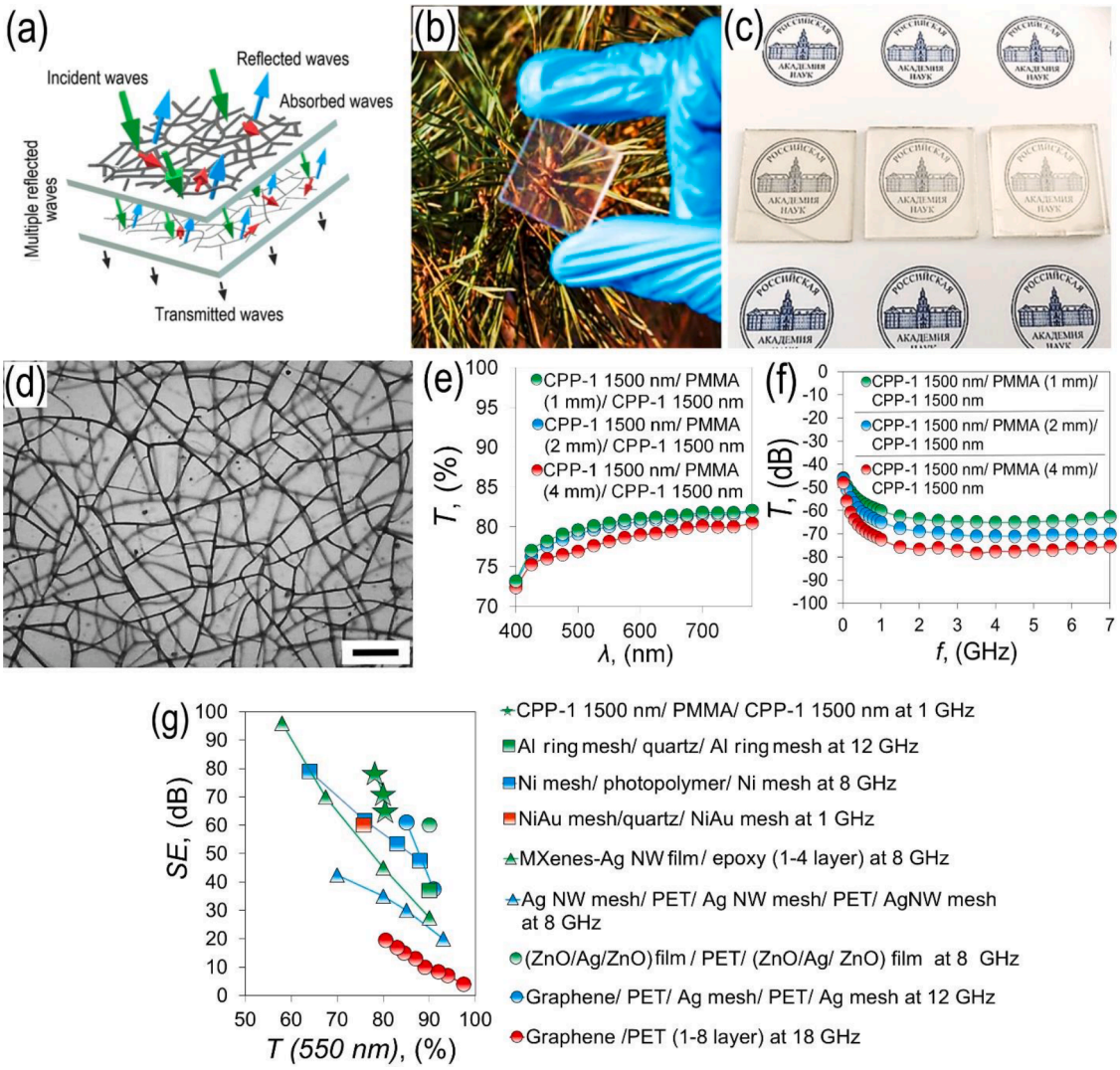

Fig. 7. Schematic representation of the interaction of electromagnetic waves with a shielding sandwich structures (a); Demonstration of the high transparency of the CPP-1 1500 nm/ PMMA (4 mm)/ CPP-1 1500 nm sample with the Pínus sibírica background (b); Photo of shielding sandwich structures based on CPP-1 1500 nm Ag meshes with PMMA spacers of various thicknesses (c); Micro image of CPP-1 1500 nm/ PMMA (4 mm)/ CPP-1 1500 nm sandwich structure on top of each other (d); Transmittance spectra of sandwich structures with different PMMA spacer thicknesses (e); Spectral transmission in the range 0.01–7 GHz for sandwich structures based on CPP-1 1500 nm Ag meshes with PMMA spacers of various thicknesses (f); Comparison of SE sandwich structures CPP-1 1500/ PMMA/ CPP-1 1500 with literature results in the form of sandwich structures based on PL template: Ni mesh/photopolymer/ Ni mesh [60]; Al ring mesh/quatz/ Al ring mesh [61]; laser etched NiAu mesh/ quartz/ NiAu mesh [62]; Ag NW mesh/ PET (3 layer) [63]; MXenes-Ag NW/ epoxy (1–4 layers) [66]; ZnO/ Ag/ ZnO/ PET/ ZnO/ Ag/ ZnO film [67], graphene/PET (1–8 layers) [68] (g).

of the interaction of an electromagnetic wave with a shielding sandwich structure. In addition to the successive attenuation of the wave of each of the Ag meshes, losses associated with multiple internal reflections are observed in sandwich structures.

In this work, we consider shielding sandwich structures, which consisted of the following layers, as a transparent conductor, we chose Ag meshes CPP-1 1500 nm, since they have the best balance between transparency and *SE*, according to the above studies, the resistance of such coatings was 1.59 Ω/sq, the optical transparency was 89.1%. To separate two Ag meshes of the same type, PMMA spacers with a thickness of 1, 2, and 4 mm were used. The appearance of shielding sandwich structures and a demonstration of their high transparency are shown in Fig. 7b and c.

The irregular Ag mesh based cracked template structure in sandwich geometry does not have moiré patterns and other optical artifacts associated with light diffraction, which are typical for square, hexagonal and other regular meshes. On Fig. 7d is a photomicrograph of two Ag meshes CPP-1 1500 nm superimposed on each other. On Fig. 7e shows the spectral dependence of optical transmission for sandwich structures with different PMMA spacer thicknesses. As for single-layer Ag mesh transparent conductors, we do not take into account the reflection from the substrate boundaries in the given spectra. The spectral transmission of PET/ PMMA/ PET structures with different PMMA spacer thicknesses are shown in Fig. S8. The resulting shielding sandwich structures have an optical transmission of 80.45% for a 1 mm thick PMMA spacer, 80.02% for a 2 mm thick PMMA spacer, and 78.14% for a 4 mm thick PMMA spacer. Increasing the spacer thickness leads to a slight decrease in optical transmission. In the range of 400–550 nm, a decrease in optical transmission is observed for all types of sandwich structures, which is most likely caused by Rayleigh light scattering.

Fig. 7f shows the spectral dependence of the coefficient *T*; in the range from 10 MHz to 1 GHz, a decrease in *T* is observed, and hence an increase in *SE*. In the range of 1–7 GHz, sandwich structures demonstrate an almost constant value of *T* with a small local minimum at 3.5 GHz. This behavior of the *T* spectra is characteristic of all samples under consideration. An increase in the spacer thickness in shielding sandwich

structures leads to a consistent increase in the maximum *SE* value, which takes the values of 65.09 dB (1 mm PMMA spacer), 71.01 dB (2 mm PMMA spacer) and 78.35 dB (4 mm PMMA spacer) at a wavelength of 3.5 GHz. The main shielding mechanism for sandwich structures, as in the case of single-layer Ag meshes, is microwave radiation reflection. A sandwich structure with a 4 mm thick PMMA spacer is a prototype of a shielding window that can be used in the design and construction of facilities with increased requirements for information protection, provides *SE* more than 78 dB in the 1–7 GHz range.

The comparative dependence of the *SE* value on the optical transmission of our sandwich structures with the literature results is shown in Fig. 7g. A comparison of the spectral dependences indicates the correctness of our measurements, since their frequency dependence is similar to the previously published results and model calculations [61]. As can be seen from the comparative dependences, two layers are enough for thick Ag meshes to provide a shielding efficiency of>70 dB while maintaining transparency above 80%. Transparent conductors such as Ag NW mesh [65] and MXenes/Ag NW hybrid films [66] require more layers due to the fact that the sheet resistance of a transparent conductor is more than 5 Ω/sq, which ultimately leads to a decrease in the balance between optical transmission and *SE*.

3.5. Adhesion strength, mechanical properties, long-term stability and their effect on EMI shielding properties

In addition to excellent optoelectric characteristics and high shielding efficiency, it is important for any coating to maintain these parameters for a long time when exposed to various stress factors. The main criteria that can be used to characterize a transparent conductor include stability to adhesive tape peeling and bending deformation with a small radius, as well as oxidation by air oxygen and water vapor, both at room and at elevated temperatures.

According to ASTM D 3359, the adhesive properties of coatings can be assessed using the tape test. The adhesion strength of the Ag mesh in our case depends on the energy of interaction between the adhesion Cr film and the PET substrate. The interaction between the substrate and Cr depends on the sputtering mode and thermal load. The geometrical parameters of the Ag mesh, such as the thickness and width of the track, also affect the adhesive properties of the coating. Fig. 8 shows photomicrographs of the same element of the notch lattice before the tape test, after one cycle and after 100 cycles, respectively, for Ag meshes w/o CPP 1000 nm. We see an absolutely identical Ag mesh for all three photographs (Fig. 8a) therefore, this mesh can be assigned to the 5th class of adhesive strength. For Ag meshes CPP-2 2500 nm, a damaged path (marked with a red circle) was observed after the notching lattice step, after one tape test cycle we did not observe visible changes, however, after 100 tape test cycles we saw an increase in the damaged area (Fig. 8b). It is fair to attribute Ag meshes CPP-2 2500 nm to the 4th class of adhesive strength. Fig. 8c shows a histogram of the adhesive strength value according to ASTM D 3359, with the exception of CPP-2 2500 nm which we assigned to the adhesive strength class 4, all other coatings belong to the adhesive strength class 5, then examination by optical microscopy of the testing area did not show peeling more than 5% of the entire study area.

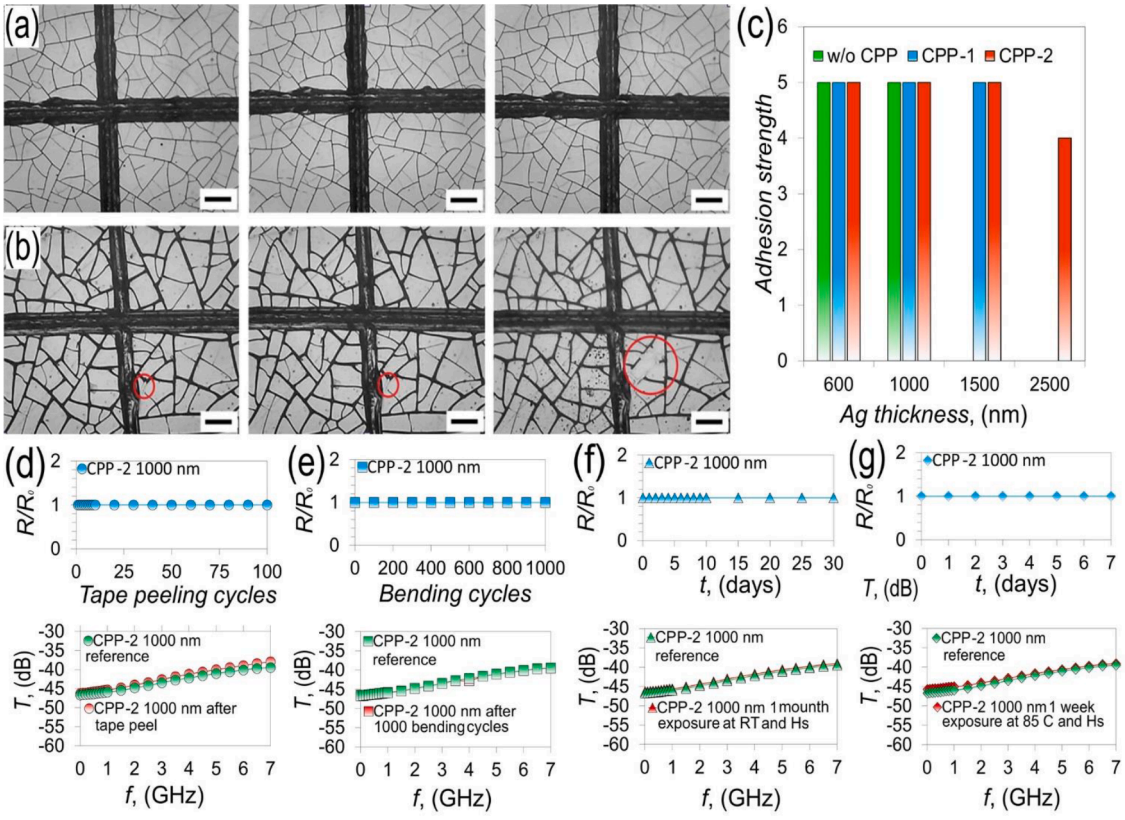

Fig. 8. Microphotographs of samples w/o CPP 1000 nm before tape test, after 10 cycles of tape test and after 100 cycles of tape test, respectively (a); Microphotographs of CPP-2 2500 nm samples before tape test, after 10 tape test cycles, and after 100 tape test cycles, respectively (b); Overall tape test results for Ag meshes based on templates w/o CPP, CPP-1 and CPP-2 at various silver sputtering thicknesses (c); Dependence of the absolute sheet resistance of Ag mesh CPP-2 1000 nm on the number of tape peeling cycles and *T* spectra before and after 100 tape peeling cycles (d); Dependence of the absolute sheet resistance of Ag mesh CPP-2 1000 nm on the number of bending cycles with a radius of 5 mm and *T* before and after 1000 bending cycles (e); Dependence of the absolute sheet resistance of Ag mesh CPP-2 1000 nm on the exposure time at room temperature and saturated humidity and *T* before and after one month exposure under given conditions (f); Dependence of the absolute sheet resistance of Ag mesh CPP-2 1000 nm on exposure time at 85 °C and saturated humidity and *T* before and after one month exposure under given conditions (g).

For transparent shielding films, it is important to study the effect of various stress factors on the sheet resistance and *SE* of Ag meshes. Tape peeling, bending, and exposure to saturated humidity and high temperature for a long time were chosen as stress factors. For these studies, 5 independent samples of Ag meshes CPP-2 1000 nm were used.

Fig. 8d shows the dependence of the absolute sheet resistance on the number of tape peeling cycles. The above analysis shows that our Ag meshes have a strong adhesion to the substrate, the measurement of sheet resistance also showed no change in the behavior of the coating after 100 tape peeling cycles. If we compare the *T* spectra for Ag meshes CPP-2 1000 nm before and after 100 cycles of tape peeling, we can see a discrepancy in the spectra. In particular, at a frequency of 10 MHz, the difference between the spectra is 0.43 dB, while at a frequency of 7 GHz it increases to 1.55 dB. It can be assumed that this is due to a small delamination of the mesh segment, as a result of which the average cells size has changed locally, which can be considered as an aperture with a large linear size.

Fig. 8e shows the dependence of sheet resistance on the number of bending cycles, with a radius of 5 mm. It can be seen that 1000 cycles do not lead to a change in sheet resistance. This high flexural resistance results from two factors. First, Ag mesh has high ductility and resistance to fatigue stress accumulation, which was previously described in the literature [69]. Secondly, we used a PET substrate with a thickness of 50 μm, and, as is known, the thickness of the substrate is proportional to the amount of film deformation during bending [70]. The spectral dependence of SE for the reference sample and the sample after 1000 bending cycles are identical.

We carried out climatic tests in two modes, at a temperature of 20 °C (Fig. 8f) and 85 °C (Fig. 8g) with saturated humidity, which led to condensation on the surface of the Ag mesh. In both cases, there was no change in sheet resistance over the entire observation period. The following conclusion can be drawn: thick Ag meshes based on a cracked template with peeling of the cells perimeter demonstrate stability to corrosive effects of air oxygen and water vapor. The spectral dependences of *T* in both cases are identical to the reference Ag mesh CPP-2 1000 nm. It can be noted that thick Ag meshes have excellent oxidation stability, significantly exceeding those of Ag and Cu NW films, as well as thin metal mesh transparent conductors, which, as a rule, require passivation layers to protect against the corrosive effects of oxygen and water vapor. The following materials have been proposed as passivating layers: graphene [26], MXenes [66,71], thin polymer films, for example, PMMA [20], PES [19,22], epoxy resin [72], TCO [73], all these types of passivating layers demonstrate a significant increase in corrosion stability both in the case of Ag and Cu NW`s, and in the case of thin Ag meshes.

4. Conclusion

We have demonstrated for the first time the possibility of controlled peeling of the cells perimeter of cracked template. Peeling of the cells perimeter occurs during the relaxation of mechanical stresses that accumulate during successive iterations of moistening and shock drying. A cracked template with a partially peeled cell perimeter makes it possible to obtain an Ag mesh transparent conductor with a thickness of more than 1 μm by magnetron sputtering. Such a result has not been previously demonstrated in the literature. The high efficiency of shielding of microwave radiation in the range of 0.01–7 GHz is shown. Thick Ag meshes based on cracked template with peeled cells perimeter demonstrate excellent stability under various stress tests, as well as maintaining the original shielding parameters. Thick Ag meshes based on cracked template, due to the excellent balance between optical transmission and *SE*, are excellent candidates for shielding sandwich structures, demonstrating *SE* 71.01 dB at a transparency of 80.02% with no optical artifacts characteristic of regular mesh transparent conductors.

CRediT authorship contribution statement

A.S. Voronin: Conceptualization, Methodology, Investigation, Writing – original draft, Visualization. **Y.V. Fadeev:** Investigation, Methodology, Validation. **F.S. Ivanchenko:** Conceptualization, Methodology, Investigation. **S.S. Dobrosmyslov:** Investigation. **M.O. Makeev:** Investigation, Visualization, Writing – review & editing. **P.A. Mikhalev:** Investigation, Supervision, Funding acquisition. **A.S. Osipkov:** Investigation, Supervision, Funding acquisition. **I.A. Damaratsky:** Investigation, Writing – review & editing. **D.S. Ryzhenko:** Investigation, Supervision. **G.Y. Yurkov:** Investigation, Supervision. **M.M. Simunin:** Methodology, Investigation. **M.N. Volochaev:** Visualization. **I.A. Tambasov:** Investigation. **S.V. Nedelin:** Investigation. **N.A. Zolotovsky:** Investigation. **D.D. Bainov:** Investigation. **S.V. Khartov:** Conceptualization, Methodology, Supervision, Funding acquisition.

Declaration of Competing Interest

The authors declare that they have no known competing financial interests or personal relationships that could have appeared to influence the work reported in this paper.

Data availability

Data will be made available on request.

Acknowledgments

The development of the processes of synthesis of a cracked template and conceptualization and optimization parameters peeling cells perimeter of the cracked template for the requirements of the final products were carried out with the financial support of the Ministry of Science and Higher Education of the Russian Federation within the framework of state task No. 0287–2021–0026. The development of the processes of the formation of metal films and the study of the structural, optical, electrical and shielding properties of the samples were carried out with the financial support of the Ministry of Science and Higher Education of the Russian Federation within the framework of state assignment No. FSFN-2022–0007. The physicochemical analysis of materials was carried out on equipment from the Krasnoyarsk Regional Center of Research Equipment of Federal Research Center «Krasnoyarsk Science Center SB RAS». We would like to thank Anastasia Tamarovskaya for the macro photo of thick Ag mesh samples.

References

[1] D.O. Carpenter, Human disease resulting from exposure to electromagnetic fields, Rev. Env. Health. 28 (2013) 159–172, https://doi.org/10.1515/reveh-2013-0016.
[2] C. Hu, H. Zuo, Y. Li, Effects of radiofrequency electromagnetic radiation on neurotransmitters in the brain, Front. Pub. Health 9 (2021), 691880, https://doi.org/10.3389/fpubh.2021.691880.
[3] X.Y. Wang, S.Y. Liao, Y.J. Wan, P.L. Zhu, Y.G. Hu, T. Zhao, R. Sun, C.P. Wong, Electromagnetic interference shielding materials: recent progress, structure design, and future perspective, J. Mater. Chem. C 10 (2022) 44–72, https://doi.org/10.1039/D1TC04702G.
[4] S. Geetha, K.K.S. Kumar, C.R.K. Rao, M. Vijayan, D.C. Trivedi, E.M.I. Shielding, Methods and materials-a review, J. Appl. Polym. Sci. 112 (2009) 2073–2086, https://doi.org/10.1002/app.29812.
[5] D. Tan, C. Jiang, Q. Li, S. Bi, X. Wang, J. Song, Development and current situation of flexible and transparent EM shielding materials, J. Mater. Sci. -Mater. Electron. 32 (2021) 25603–25630, https://doi.org/10.1007/s10854-021-05409-4.
[6] Z. Liang, Z. Zhao, M. Pu, J. Luo, X. Xie, Y. Wang, Y. Guo, X. Ma, X. Luo, Metallic nanomesh for high-performance transparent electromagnetic shielding, Opt. Mater. Express. 10 (2020) 796–806, https://doi.org/10.1364/OME.386830.
[7] W. Wang, B. Bai, Q. Zhou, K. Ni, H. Lin, Petal-shaped metallic mesh with high electromagnetic shielding efficiency and smoothed uniform diffraction, Opt. Mater. Express. 8 (2018) 3485–3493, https://doi.org/10.1364/OME.8.003485.
[8] J. Tan, Z. Lu, Contiguous metallic rings: an inductive mesh with high transmissivity, strong electromagnetic shielding, and uniformly distributed stray light, Opt. Express. 15 (2007) 790–796, https://doi.org/10.1364/OE.15.000790.

[9] H. Wang, Z. Lu, J. Tan, Y. Zhang, J. Cao, X. Lu, Y. Liu, R. Kong, S. Lin, Transparent conductor based on metal ring clusters interface with uniform light transmission for excellent microwave shielding, Thin Solid Films 662 (2018) 76–82, https://doi.org/10.1016/j.tsf.2018.07.038.

[10] S.I. Chung, P.K. Kim, T.G. Ha, J.T. Han, High-performance flexible transparent nanomesh electrodes, Nanotechnology 30 (2019), 125301, https://doi.org/10.1088/1361-6528/aafb94.

[11] H.S. Choi, S.J. Suh, S.W. Kim, H.J. Kim, J.W. Park, Transparent electromagnetic shielding film utilizing imprinting-based micro patterning technology, Polym 13 (2021) 738, https://doi.org/10.3390/polym13050738.

[12] Y. Han, J. Lin, Y. Liu, H. Fu, Y. Ma, P. Jin, J. Tan, Crackle template based metallic mesh with highly homogeneous light transmission for high-performance transparent EMI shielding, Sci. Rep. 6 (2016) 25601, https://doi.org/10.1038/srep25601.

[13] V.V. Tran, D.D. Nguyen, A.T. Nguyen, M. Hofmann, Y.P. Hsieh, H.C. Kan, C.C. Hsu, Electromagnetic interference shielding by transparent graphene/nickel mesh films, ACS Appl. Nano Mater. 3 (2020) 7474–7481, https://doi.org/10.1021/acsanm.0c01076.

[14] A.S. Voronin, Yu.V. Fadeev, I.V. Govorun, A.S. Voloshin, I.A. Tambasov, M. M. Simunin, S.V. Khartov, A transparent radio frequency shielding coating obtained using a self-organized template, Tech. Phys. Lett. 47 (2021) 259–262, https://doi.org/10.1134/S1063785021030159.

[15] M.H. Kim, H. Joh, S.H. Hong, S.J. Oh, Coupled Ag nanocrystal-based transparent mesh electrodes for transparent and flexible electro-magnetic interference shielding films, Curr. Appl. Phys. 19 (2019) 8–13, https://doi.org/10.1016/j.cap.2018.10.016.

[16] K. Chizari, M. Arjmand, Z. Liu, U. Sundararaj, D. Therriault, Three-dimensional printing of highly conductive polymer nanocomposites for EMI shielding applications, Mater. Today. Commun. 11 (2017) 112–118, https://doi.org/10.1016/j.mtcomm.2017.02.006.

[17] H. Li, Y. Zhang, Y. Tai, X. Zhu, X. Qi, L. Zhou, Z. Li, H. Lan, Flexible transparent electromagnetic interference shielding films with silver mesh fabricated using electric-field-driven microscale 3D printing, Opt. Laser Tech. 148 (2022), 107717, https://doi.org/10.1016/j.optlastec.2021.107717.

[18] S.K. Vishwanath, D.G. Kim, J. Kim, Electromagnetic interference shielding effectiveness of invisible metal-mesh prepared by electrohydrodynamic jet printing, Jpn. J. Appl. Phys. 53 (2014) 05HB11, https://doi.org/10.7567/JJAP.53.05HB11.

[19] M. Hu, J. Gao, Y. Dong, K. Li, G. Shan, S. Yang, R.K.Y. Li, Flexible transparent PES/silver nanowires/PET sandwich-structured film for high-efficiency electromagnetic interference shielding, Langmuir 28 (2012) 7101–7106, https://doi.org/10.1021/la300720y.

[20] X. Zhu, A. Guo, Z. Yan, F. Qin, J. Xu, Y. Ji, C. Kan, PET/Ag NW/PMMA transparent electromagnetic interference shielding films with high stability and flexibility, Nanoscale 13 (2021) 8067, https://doi.org/10.1021/acsami.7b14626.

[21] L.C. Jia, D.X. Yan, X.F. Liu, R.J. Ma, H.Y. Wu, Z.M. Li, Highly efficient and reliable transparent electromagnetic interference shielding film, ACS Appl. Mater. Interfaces 10 (2018) 11941–11949, https://doi.org/10.1021/acsami.8b00492.

[22] Q. Xie, Z. Yan, S. Wang, Y. Wang, L. Mei, F. Qin, R. Jiang, Transparent, flexible, and stable polyethersulfone/copper-nanowires/polyethylene terephthalate sandwich-structured films for high-performance electromagnetic interference shielding, Adv. Eng. Mater. 23 (2021), 2100283, https://doi.org/10.1002/adem.202100283.

[23] H. Wang, C. Ji, C. Zhang, Y. Zhang, Z. Zhang, Z. Lu, J. Tan, L.J. Guo, Highly transparent and broadband electromagnetic interference shielding based on ultrathin doped Ag and conducting oxides hybrid film structures, ACS Appl. Mater. Interfaces 11 (2019) 11782–11791, https://doi.org/10.1021/acsami.9b00716.

[24] R.A. Maniyara, V.K. Mkhitaryan, T.L. Chen, D.S. Ghosh, V. Pruneri, An antireflection transparent conductor with ultralow optical loss (<2%) and electrical resistance (<6 Ω sq−1), Nat. Commun. 7 (2016) 13771, https://doi.org/10.1038/ncomms13771.

[25] P. Kumar, P.V. Reddy, B. Choudhury, P. Chowdhury, H.C. Barshilia, Transparent conductive Ta/Al/Ta-grid electrode for optoelectronic and electromagnetic interference shielding applications, Thin Solid Films 612 (2016) 350–357, https://doi.org/10.1016/j.tsf.2016.06.010.

[26] Y. Han, Y. Liu, L. Han, J. Lin, Jin High-performance hierarchical graphene/metal-mesh film for optically transparent electromagnetic interference shielding, Carbon 115 (2017) 34–42, https://doi.org/10.1016/j.carbon.2016.12.092.

[27] N. Bönninghoff, J.P. Chua, C.W. Chang, M. Mehretie, B.Z. Lai, Preparation and characterization of micron-scale molybdenum metal mesh electrodes, Surf. Coat. Technol 349 (2018) 224–232, https://doi.org/10.1016/j.surfcoat.2018.03.085.

[28] K. Shi, J. Su, K. Hu, H. Liang, High-performance copper mesh for optically transparent electromagnetic interference shielding, J. Mater. Sci. - Mater. Electron. 31 (2020) 11646–11653, https://doi.org/10.1007/s10854-020-03716-w.

[29] S. Shen, S.Y. Chen, D.Y. Zhang, Y.H. Liu, High-performance composite Ag-Ni mesh based flexible transparent conductive film as multifunctional devices, Opt. Express 26 (2018) 27545–27554, https://doi.org/10.1364/OE.26.027545.

[30] Q. Peng, S. Li, B. Han, Q. Rong, X. Lu, Q. Wang, M. Zeng, G. Zhou, J.M. Liu, K. Kempa, Gao, Colossal figure of merit in transparent-conducting metallic ribbon networks, Adv. Mater. Technol. 1 (2016), 1600095, https://doi.org/10.1002/admt.201600095.

[31] A.S. Voronin, Y.V. Fadeev, I.V. Govorun, I.V. Podshivalov, M.M. Simunin, I. A. Tambasov, D.V. Karpova, T.E. Smolyarova, A.V. Lukyanenko, A.A. Karacharov, I.V. Nemtsev, S.V. Khartov, Cu-Ag and Ni-Ag meshes based on cracked template as efficient transparent electromagnetic shielding coating with excellent mechanical performance, J. Mater. Sci. 56 (2021) 14741–14762, https://doi.org/10.1007/s10853-021-06206-4.

[32] A.S. Voronin, Y.V. Fadeev, M.O. Makeev, P.A. Mikhalev, A.S. Osipkov, A. S. Provatorov, D.S. Ryzhenko, G.Y. Yurkov, M.M. Simunin, D.V. Karpova, A. V. Lukyanenko, D. Kokh, D.D. Bainov, I.A. Tambasov, S.V. Nedelin, N. A. Zolotovsky, S.V. Khartov, Low cost embedded copper mesh based on cracked template for highly durability transparent EMI shielding films, Mater 15 (2022) 1449, https://doi.org/10.3390/ma15041449.

[33] L. Pauchard, Patterns caused by buckle-driven delamination in desiccated colloidal gels, Europhys. Lett. 74 (2006) 188–194, https://doi.org/10.1209/epl/i2005-10493-3.

[34] A. Kumar, G.U. Kulkarni, Time evolution and spatial hierarchy of crack patterns, Langmuir 37 (2021) 13141–13147, https://doi.org/10.1021/acs.langmuir.1c02363.

[35] S. Kiruthika, K.D.M. Rao, A. Kumar, R. Gupta, G.U. Kulkarni, Metal wire network based transparent conducting electrodes fabricated using interconnected crackled layer as template, Mater. Res. Express 1 (2014), 026301, https://doi.org/10.1088/2053-1591/1/2/026301.

[36] R. Gupta, K.D.M. Rao, K. Srivastava, A. Kumar, S. Kiruthika, G.U. Kulkarni, Spray coating of crack templates for the fabrication of transparent conductors and heaters on flat and curved surfaces, ACS Appl. Mater. Interfaces 6 (2014) 13688–13696, https://doi.org/10.1021/am503154z.

[37] C.P. Muzzillo, M.O. Reese, L.M. Mansfield, Fundamentals of using cracked film lithography to pattern transparent conductive metal grids for photovoltaics, Langmuir 36 (2020) 4630–4636, https://doi.org/10.1021/acs.langmuir.0c00276.

[38] B. Han, K. Pei, Y. Huang, X. Zhang, Q. Rong, Q. Lin, Y. Guo, T. Sun, C. Guo, D. Carnahan, M. Giersig, Y. Wang, J. Gao, Z. Ren, K. Kempa, Uniform self-forming metallic network as a high-performance transparent conductive electrode, Adv. Mater. 26 (2014) 873–877, https://doi.org/10.1002/adma.201302950.

[39] A.F. Routh, Drying of thin colloidal films, Rep. Prog. Phys. 76 (2013), 046603, https://doi.org/10.1088/0034-4885/76/4/046603.

[40] Y.Y. Tarasevich, Mechanisms and models of the dehydration self-organization in biological fluids, Phys. Usp. 47 (2004) 717, https://doi.org/10.1070/PU2004v047n07ABEH001758.

[41] S.Y. Lee, J.Y. Hwang, Transparent heater with meshed amorphous oxide/metal/amorphous oxide for electric vehicle applications, Sci. Rep. 10 (2020) 9697, https://doi.org/10.1038/s41598-020-66514-8.

[42] D.J. Kim, H.J. Kim, K.W. Seo, K.H. Kim, T.W. Kim, H.K. Kim, Indium-free, highly transparent, flexible $Cu_2O/Cu/Cu_2O$ mesh electrodes for flexible touch screen panels, Sci. Rep. 5 (2015) 16838, https://doi.org/10.1038/srep16838.

[43] Y.G. Kim, Y.J. Tak, S.P. Park, H.J. Kim, H.J. Kim, Structural engineering of metal-mesh structure applicable for transparent electrodes fabricated by self-formable cracked template, Nanomat 7 (2017) 214, https://doi.org/10.3390/nano7080214.

[44] C.F. Guo, T. Sun, Q. Liu, Z. Suo, Z. Ren, Highly stretchable and transparent nanomesh electrodes made by grain boundary lithography, Nat. Commun. 5 (2014) 3121, https://doi.org/10.1038/ncomms4121.

[45] S. Kiruthika, R. Gupta, G.U. Kulkarni, Large area defrosting windows based on electrothermal heating of highly conducting and transmitting Ag wire mesh, RSC Adv. 4 (2014) 49745–49751, https://doi.org/10.1039/C4RA06811D.

[46] X. Zhu, M. Liu, X. Qi, H. Li, Y.F. Zhang, Z. Li, Z. Peng, J. Yang, L. Qian, Q. Xu, N. Gou, J. He, D. Li, H. Lan, Templateless, plating-free fabrication of flexible transparent electrodes with embedded silver mesh by electric-field-driven microscale 3D printing and hybrid hot embossing, Adv. Mater. 33 (2021), 2007772, https://doi.org/10.1002/adma.202007772.

[47] S.J. Lee, Y.H. Kim, J.K. Kim, H. Baik, J.H. Park, J. Lee, J. Nam, J.H. Park, T.W. Lee, G.R. Yi, J.H. Cho, A roll-to-roll welding process for planarized silver nanowire electrodes, Nanoscale 6 (2014) 11828–11834, https://doi.org/10.1039/C4NR03771E.

[48] J. Jung, H. Lee, I. Ha, Highly stretchable and transparent electromagnetic interference shielding film based on silver nanowire percolation network for wearable electronics applications, ACS Appl. Mater. Interfaces 9 (2017) 44609–44616, https://doi.org/10.1021/acsami.7b14626.

[49] X. Yang, P. Gao, Z. Yang, J. Zhu, F. Huang, J. Ye, Optimizing ultrathin Ag films for high performance oxide-metal-oxide flexible transparent electrodes through surface energy modulation and template-stripping procedures, Sci. Rep. 7 (2017) 44576, https://doi.org/10.1038/srep44576.

[50] S.H. Park, S.M. Lee, E.H. Ko, T.H. Kim, Y.C. Nah, S.J. Lee, J.H. Lee, H.K. Kim, Roll-to-Roll sputtered ITO/Cu/ITO multilayer electrode for flexible, transparent thin film heaters and electrochromic applications, Sci. Rep. 6 (2016) 33868, https://doi.org/10.1038/srep33868.

[51] K. Ellmer, Past achievements and future challenges in the development of optically transparent electrodes, Nat. Photon. 6 (2012) 809–817, https://doi.org/10.1038/nphoton.2012.282.

[52] A.K. Sharma, K.K. Mishra, M. Raghuramaiah, P.A. Naik, P.D. Gupta, Design and performance characteristics of an electromagnetic interference shielded enclosure for high voltage Pockels cell switching system, Sadhana 32 (2007) 235–242, https://doi.org/10.1007/s12046-007-0020-z.

[53] H. Wang, Z. Lu, J. Tan, Generation of uniform diffraction pattern and high EMI shielding performance by metallic mesh composed of ring and rotated sub-ring arrays, Opt. Express 24 (2016) 22989–23000, https://doi.org/10.1364/OE.24.022989.

[54] A. Osipkov, M. Makeev, E. Konopleva, N. Kudrina, L. Gorobinskiy, P. Mikhalev, D. Ryzhenko, G. Yurkov, Optically transparent and highly conductive electrodes for acousto-optical devices, Mater 14 (2021) 7178, https://doi.org/10.3390/ma14237178.

[55] F. Qin, Z. Yan, J. Fan, J. Cai, X. Zhu, X. Zhang, Highly uniform and stable transparent electromagnetic interference shielding film based on silver nanowire–PEDOT:PSS composite for high power microwave shielding, Macromol. Mater. Eng. 306 (2021), 2000607, https://doi.org/10.1002/mame.202000607.
[56] D.G. Kim, J.H. Choi, D.-.K. Choi, S.W. Kim, Highly bendable and durable transparent electromagnetic interference shielding film prepared by wet sintering of silver nanowires, ACS Appl. Mater. Interfaces 10 (2018) 29730–29740, https://doi.org/10.1021/acsami.8b07054.
[57] D.H. Kim, Y. Kim, J.W. Kim, Transparent and flexible film for shielding electromagnetic interference, Mater. Des. 89 (2016) 703–707, https://doi.org/10.1016/j.matdes.2015.09.142.
[58] K. Shi, J. Su, H. Liang, K. Hu, Effect of different superimposed structures on the transparent electromagnetic interference shielding performance of graphene, J. Appl. Phys. 128 (2020), 185102, https://doi.org/10.1063/5.0016475.
[59] B.R. Kima, H.K. Lee, E. Kim, S.-.H. Lee, Intrinsic electromagnetic radiation shielding/absorbing characteristics of polyaniline-coated transparent thin films, Synth. Metals 160 (2010) 1838–1842, https://doi.org/10.1016/j.synthmet.2010.06.027.
[60] Z. Jiang, S. Zhao, W. Huang, Embedded flexible and transparent double-layer nickel-mesh for high shielding efficiency, Opt. Express 28 (2020) 26531–26542, https://doi.org/10.1364/OE.401543.
[61] H. Wang, Z. Lu, Y. Liu, Double-layer interlaced nested multi-ring array metallic mesh for high-performance transparent electromagnetic interference shielding, Opt. Lett. 42 (2017) 1620–1623, https://doi.org/10.1364/OL.42.001620.
[62] Y. Zhang, H. Dong, Q. Li, Double-layer metal mesh etched by femtosecond laser for high-performance electromagnetic interference shielding window, RSC Adv 9 (2019) 22282, https://doi.org/10.1039/C9RA03519B.
[63] Z. Lu, H. Wang, J. Tan, S. Lin, Microwave shielding enhancement of high-transparency, double-layer, submillimeter period metallic mesh, Appl. Phys. Lett. 105 (2014), 241904, https://doi.org/10.1063/1.4904466.
[64] Z. Lu, Y. Liu, H. Wang, J. Tan, Verification and improvement of equivalent refractive index models for evaluating the shielding effectiveness of high-transmittance double-layer metallic meshes, Appl. Opt. 55 (2016) 5372–5378, https://doi.org/10.1364/AO.55.005372.
[65] J. Gu, S. Hu, H. Ji, Multi-layer silver nanowire/polyethylene terephthalate mesh structure for highly efficient transparent electromagnetic interference shielding, Nanotechnology 31 (2020), 185303, https://doi.org/10.1088/1361-6528/ab6d9d.
[66] W. Chen, L.X. Liu, H.B. Zhang, Z.Z. Yu, Flexible, transparent, and conductive Ti3C2Tx MXene–silver nanowire films with smart acoustic sensitivity for high-performance electromagnetic interference shielding, ACS Nano 14 (2020) 16643–16653, https://doi.org/10.1021/acsnano.0c01635.
[67] C. Yuan, J. Huang, Y. Dong, X. Huang, Y. Lu, J. Li, T. Tian, W. Liu, W. Song, Record-high transparent electromagnetic interference shielding achieved by simultaneous microwave Fabry–Pérot interference and optical antireflection, ACS Appl. Mater. Interfaces 12 (2020) 26659–26669, https://doi.org/10.1021/acsami.0c05334.
[68] Z. Lu, L. Ma, J. Tan, H. Wang, X. Ding, Transparent multi-layer graphene/polyethylene terephthalate structures with excellent microwave absorption and electromagnetic interference shielding performance, Nanoscale 8 (2016) 16684–16693, https://doi.org/10.1039/C6NR02619B.
[69] W.L. Jeong, J.H. Min, H.M. Kwak, Y.J. Jeon, H.J. Lee, K.P. Kim, J.S. Lee, S.J. Kang, D.Y. Kim, D.S. Lee, A highly conductive and flexible metal mesh/ultrathin ITO hybrid transparent electrode fabricated using low-temperature crystallization, J. Alloy. Compd. 794 (2019) 114–119, https://doi.org/10.1016/j.jallcom.2019.04.249.
[70] J.H. Choi, K.Y. Lee, S.W. Kim, Ultra-bendable and durable Graphene–Urethane composite/silver nanowire film for flexible transparent electrodes and electromagnetic-interference shielding, Compos. Part B 177 (2019), 107406, https://doi.org/10.1016/j.compositesb.2019.107406.
[71] S. Bai, X. Guo, X. Zhang, X. Zhao, H. Yang, Ti3C2Tx MXene-AgNW composite flexible transparent conductive films for EMI shielding, Compos Part A 149 (2021), 106545, https://doi.org/10.1016/j.compositesa.2021.106545.
[72] L. Miao, G.J. Liu, K. McEleney, J.D. Wang, Epoxy-embedded silver nanowire meshes for transparent flexible electrodes, J. Mater. Sci. 54 (2019) 10355–10370, https://doi.org/10.1007/s10853-019-03507-7.
[73] A.K. Singh, R.K. Govind, S. Kiruthika, M.G. Sreenivasan, G.U. Kulkarni, Hybrid transparent conducting glasses made of metal nanomesh coated with metal oxide overlayer, Mater. Chem. Phys. 239 (2020), 121997, https://doi.org/10.1016/j.matchemphys.2019.121997.